

# Multi-Scenario Highway Lane-Change Intention Prediction: A Temporal Physics-Informed Multi-Modal Framework

Jiazhao Shi<sup>\*a</sup>, Ziyu Wang<sup>b</sup>, Yichen Lin<sup>a</sup>, Shoufeng Lu<sup>c</sup>

<sup>a</sup>Tandon School of Engineering, New York University, 6 MetroTech Center, Brooklyn, NY 11201, USA; <sup>b</sup>School of Business, Wake Forest University, 1834 Wake Forest Rd, Winston-Salem, NC 27109, USA; <sup>c</sup>College of Transportation Engineering, Nanjing Tech University, 30 Puzhu South Road, Nanjing, Jiangsu 211816, China  
<sup>\*</sup>js12624@nyu.edu

## ABSTRACT

Lane-change intention prediction is safety-critical for autonomous driving and ADAS, but remains difficult in naturalistic traffic due to noisy kinematics, severe class imbalance, and limited generalization across heterogeneous highway scenarios. We propose Temporal Physics-Informed AI (TPI-AI), a hybrid framework that fuses deep temporal representations with physics-inspired interaction cues. A two-layer bidirectional LSTM (Bi-LSTM) encoder learns compact embeddings from multi-step trajectory histories; we concatenate these embeddings with kinematics-, safety-, and interaction-aware features (e.g., headway, TTC, and safe-gap indicators) and train a LightGBM classifier for three-class intention recognition (No-LC, Left-LC, Right-LC). To improve minority-class reliability, we apply imbalance-aware optimization including resampling/weighting and fold-wise threshold calibration. Experiments on two large-scale drone-based datasets, highD (straight highways) and exiD (ramp-rich environments), use location-based splits and evaluate prediction horizons  $T = 1, 2, 3$  s. TPI-AI outperforms standalone LightGBM and Bi-LSTM baselines, achieving macro-F1 of 0.9562, 0.9124, 0.8345 on highD and 0.9247, 0.8197, 0.7605 on exiD at  $T = 1, 2, 3$  s, respectively. These results show that combining physics-informed interaction features with learned temporal embeddings yields robust multi-scenario lane-change intention prediction.

**Keywords:** Lane-change intention prediction, Physics-Informed AI, Autonomous driving, highD dataset, exiD dataset, Class imbalance, Deep Learning.

## 1. INTRODUCTION

Lane-changing is a high-impact driving maneuver that is tightly coupled with crash/near-crash risk, especially under dense traffic and limited driver/AV reaction time. In U.S. crash data, lane-change/merge scenarios constitute a large two-vehicle crash population and exhibit several recurring pre-crash patterns, motivating proactive prediction rather than reactive response [1].

Early studies on lane-changing behavior primarily relied on rule-based or parametric models that formalize driver decision-making under surrounding-vehicle interactions and gap acceptance [2]. For instance, Kesting *et al.* proposed the MOBIL model, which expresses lane-change decisions through an interpretable incentive–safety tradeoff based on the braking impacts imposed on neighboring vehicles [3]. While such models are transparent and encode domain constraints, they often depend on simplifying assumptions and calibration, which can limit generalization across heterogeneous traffic regimes [4]. To bridge this gap, learning-based intention prediction has gained attention by leveraging trajectory histories and interaction context directly; for example, Qi *et al.* developed an online inference approach that models lane-change event evolution with an analytical diffusion process, enabling more adaptive intention estimation for connected/automated driving settings [5].

Recent progress in deep learning has further improved the modeling of temporal dependencies and motion patterns. For instance, Izquierdo *et al.* validated a lane-change intention prediction pipeline using action-recognition networks on a temporal “motion history” representation: a GoogLeNet-based classifier achieved 0.866 accuracy for intention classification (change vs. no-change), while a GoogLeNet+LSTM model reached 0.745 accuracy for multi-class prediction (keep/left/right) under their setting [6]. Shi and Zhang proposed an LSTM-based approach tailored to imbalanced lane-change data by integrating resampling with ensemble-style training to better preserve temporal information and improve

minority-class detection [7]. These studies collectively indicate that (i) richer temporal representations help, and (ii) class imbalance is a central bottleneck for reliable early prediction.

Despite these advancements, several limitations remain:

1. **Feature representation gap between kinematics and learning.** Pure deep models can learn expressive temporal patterns but may underutilize well-established physics- and safety-inspired indicators (e.g., TTC/headway) that compactly summarize interaction risk and driver intent precursors [8], [9].
2. **Class imbalance and early-horizon reliability.** Naturalistic trajectory datasets are dominated by lane-keeping, while left/right lane-change classes are rare; models trained naively tend to overfit the majority class and degrade sharply as the prediction horizon increases [7].
3. **Generalization across traffic regimes.** Highway and urban arterial data differ in interaction complexity and uncertainty; a method that works well in one scenario may not transfer without a principled fusion of temporal cues and interaction-aware physical descriptors.

To address these issues, we propose a Temporal Physics-Informed AI (TPI-AI) framework for lane-change intention prediction. The key idea is to use a Bi-LSTM encoder to learn high-level temporal embeddings from raw multi-step trajectory histories, then concatenate these embeddings with physics-inspired interaction features and train a LightGBM-based gradient boosting classifier for final intention classification. The hybrid design aims to combine the temporal modeling strength of recurrent networks with the strong tabular decision boundaries and robustness of gradient boosting [10], [11]. The main contributions of this paper are as follows:

1. **A temporal physics-informed hybrid framework for lane-change intention prediction.** We propose TPI-AI, which fuses learned temporal embeddings (from a Bi-LSTM encoder) with physics-inspired interaction and safety features, and performs final three-class intent recognition using a LightGBM classifier.
2. **A consistent three-class formulation across heterogeneous highway scenarios.** We model lane-change intention as No-LC / Left-LC / Right-LC and provide scenario-aware labeling logic that remains applicable to both straight-road segments and ramp merging/diverging areas (where lane identifiers may be non-sequential). On highD, the hybrid approach achieves macro-F1 of 0.9562 / 0.9124 / 0.8345 at horizons T = 1 / 2 / 3 s, compared with 0.9359 / 0.8714 / 0.7823 (LightGBM) and 0.9244 / 0.8916 / 0.8115 (Bi-LSTM). On exiD, the hybrid model reaches 0.9247 / 0.8197 / 0.7605, exceeding 0.9004 / 0.8084 / 0.7127 (LightGBM) and 0.7702 / 0.7004 / 0.5840 (Bi-LSTM).
3. **A systematic multi-scenario evaluation protocol with strict generalization testing.** We conduct controlled experiments across multiple history-window lengths and prediction horizons, and adopt a location-based split to avoid trajectory overlap between train and test, evaluating the method on both straight-highway (highD) and ramp-rich (exiD) environments.

In summary, the proposed TPI-AI framework integrates temporal sequence modeling with physics-informed interaction cues and imbalance-aware calibration, delivering robust three-class lane-change intention prediction that generalizes across both straight-highway and ramp scenarios.

## 2. METHODS

### 2.1. Temporal Physics-Informed AI framework

This study proposes a Temporal Physics-Informed AI framework (Figure 1) that systematically embeds domain knowledge from vehicle kinematics, traffic safety, and roadway dynamics into a hybrid learning pipeline. As a primary innovation of this work, the framework integrates (i) physics-guided, interpretable feature construction and (ii) deep temporal representation learning from raw trajectories, and then combines them within a unified prediction model. Specifically, we first derive physically meaningful features that reflect motion dynamics and interaction feasibility, and in parallel use a two-layer bidirectional LSTM (Bi-LSTM) encoder to extract high-level temporal representations from sequential trajectory observations. These learned temporal features are then fused with the traditional physics-guided features and fed into a LightGBM classifier for lane-change intention recognition. Compared with purely data-driven approaches, this design injects physical plausibility and safety-relevant structure while retaining the expressive power of deep temporal modeling, leading to improved generalization, stability, and interpretability across diverse highway scenarios.

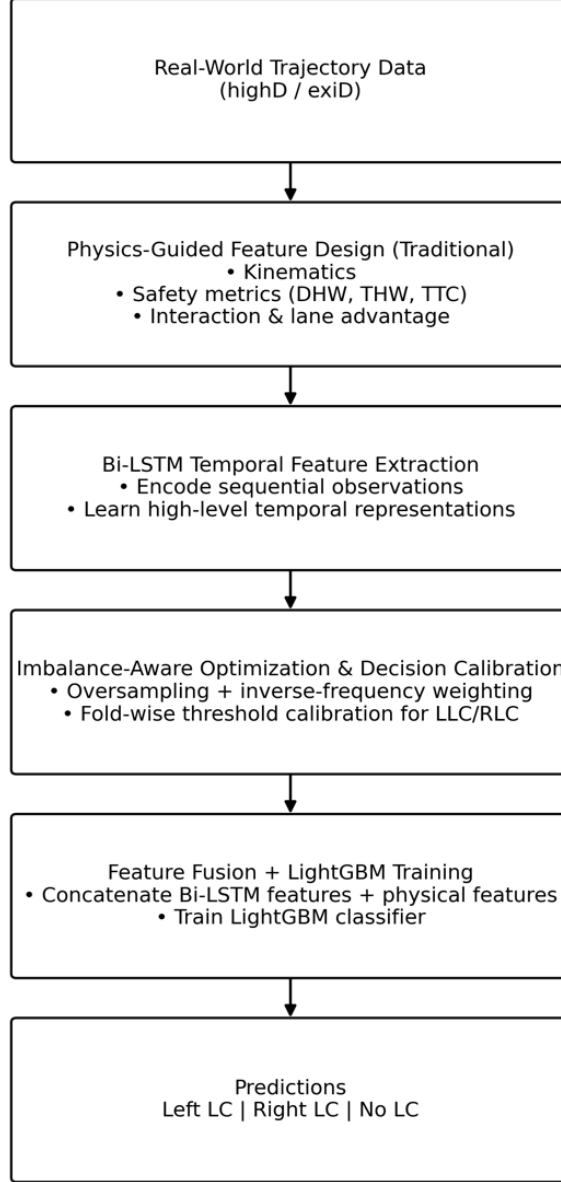


Figure 1. Structural diagram of the proposed Temporal physics-informed AI framework.

The framework consists of four interconnected components, guiding the process from data preparation and problem formulation to model training and prediction:

1. **Physics-Guided Feature Design and Lane-Change Formulation.** The input space is extended beyond raw trajectory data through the inclusion of features derived from domain knowledge. This includes vehicle kinematics (e.g., speed, acceleration, yaw rate), longitudinal safety metrics such as Distance Headway (DHW), Time Headway (THW), and Time-to-Collision (TTC), as well as interaction-aware indicators like safe gap availability and lane-advantage indices. These features capture the dynamic context and risk landscape surrounding the ego vehicle, providing a physically meaningful basis for maneuver prediction. The detailed definitions and computations of these features are elaborated in Section 3.3. Within this physics-informed context, we formulate lane-change intention as a three-class classification problem, distinguishing between “left lane change,” “right lane change,” and “no lane change.” The definitions for these maneuvers are established as follows, tailored to different highway scenarios using the highD and exiD datasets:

### a. Straight Road Scenarios

Figure 2 illustrates a lane-change event on a straight roadway.

Start Time: The lateral position crosses the current lane centerline by at least 0.2 m, followed by monotonic lateral drift for at least 0.5 s.

End time: The vehicle is fully within the adjacent lane, with no reverse lateral motion for at least 1.0 s afterward.

Direction: Assuming the driving direction is unchanged, the maneuver is labeled left if the laneId before the change is less than that after the change, and right otherwise (in highD, lane indices increase from left to right within each travel direction).

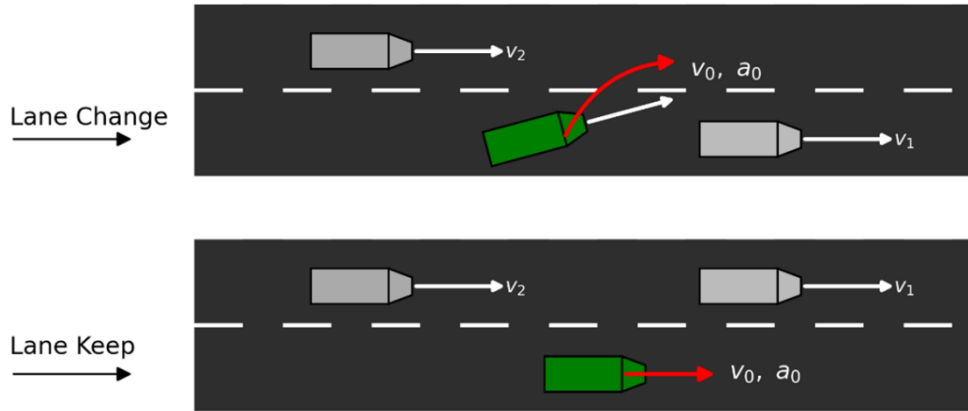


Figure 2. Straight road scenarios (based on highD dataset).

### b. Ramp Merging/Diverging Scenarios

Figure 3 illustrates a lane-change event in a ramp area.

Start time: The lateral position crosses the lane centerline by at least 0.2 m, followed by monotonic lateral drift for at least 0.5 s.

End time: The vehicle is fully within the adjacent lane, with no reverse lateral motion for at least 1.0 s afterward.

Direction: Because laneId is not sequential between mainline lanes and ramps in exiD, direction is inferred from lateral velocity. Specifically, latVelocity is averaged over a 0.1 s window starting at the start time; a positive mean indicates left, otherwise right.

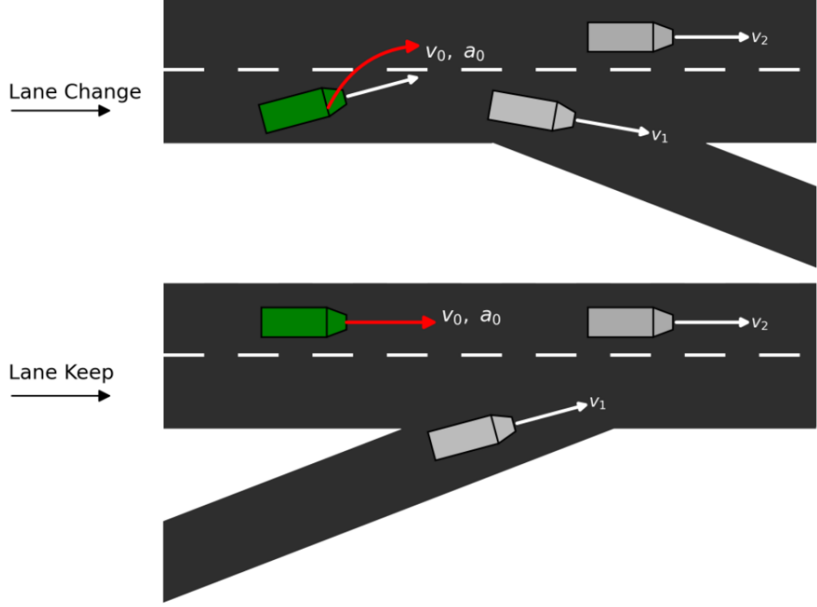


Figure 3. Ramp merging/diverging scenarios (based on exiD dataset).

2. **Bi-LSTM Temporal Feature Extraction from Raw Trajectories.** In addition to handcrafted physical features, we employ a two-layer bidirectional LSTM (Bi-LSTM) encoder to learn compact high-level temporal representations from sequential trajectory observations. By modeling both forward and backward temporal dependencies, the Bi-LSTM captures maneuver-relevant patterns that may be difficult to fully express through instantaneous physical variables alone, such as evolving lateral intent, gradual drift, and interaction-driven adjustments over time. The resulting embedding serves as a learned summary of the trajectory’s temporal dynamics and complements the physics-guided feature set.
3. **Imbalance-Aware Optimization and Decision Calibration.** To address class skew and operating-point sensitivity, we combine oversampling and inverse-frequency weighting with fold-wise threshold calibration for minority classes (LLC/RLC) strictly within cross-validation. This improves macro-F1 and minority-class recall while avoiding leakage, and yields more reliable decision boundaries for practical deployment.
4. **Feature Fusion + LightGBM Training.** We fuse the learned Bi-LSTM temporal representations with the traditional physics-guided features (via feature concatenation) and train a LightGBM classifier for three-class lane-change intention recognition. This hybrid modeling strategy leverages the interpretability and robustness of gradient-boosted trees while enriching the input with deep temporal features learned directly from sequential data. The result is a unified predictor that benefits from both physically grounded signals and high-level temporal dynamics.

By unifying physics-guided formulation, Bi-LSTM-based temporal representation learning, imbalance-aware calibration, and fused LightGBM training within a single temporal physics-informed paradigm, the proposed framework bridges the gap between domain knowledge and data-driven learning. The subsequent sections (2.2–2.4) detail the algorithmic modules (two-layer Bi-LSTM encoder and LightGBM classifier) instantiated within this overarching framework, resulting in a more robust and interpretable lane-change intention recognition method suitable for real-world autonomous driving systems.

## 2.2. LightGBM

LightGBM (Light Gradient Boosting Machine) is a gradient-boosted decision tree implementation optimized for speed and scalability via two design choices: **histogram-based split finding** and **leaf-wise tree expansion**. Instead of searching split points over the full continuous feature domain, LightGBM first maps each continuous feature into a small set of discrete bins. Split evaluation is then performed on these binned values, which reduces both memory usage and computational cost while retaining the second-order optimization behavior of modern GBDT training.

Concretely, for a feature  $k$  and its histogram bin  $v$ , LightGBM aggregates node-level first- and second-order statistics by summing gradients and Hessians of samples whose feature values fall within the bin range:

$$G_{k,v} = \sum_{j \in \{j | s_{k,v} \geq x_{jk} > s_{k,v-1}\}} g_j, \quad H_{k,v} = \sum_{j \in \{j | s_{k,v} \geq x_{jk} > s_{k,v-1}\}} h_j \quad (1)$$

Here,  $G_{k,v}$  and  $H_{k,v}$  represent the cumulative gradients and Hessians for bin  $v$  of feature  $k$ . This histogram-based aggregation allows for rapid evaluation of split gains, where the gain formula remains consistent with that in GBDT:

$$Gain = \frac{1}{2} \left( \frac{G_L^2}{H_L + \lambda} + \frac{G_R^2}{H_R + \lambda} - \frac{(G_L + G_R)^2}{H_L + H_R + \lambda} \right) - \gamma \quad (2)$$

With  $G = \sum g_i$  and  $H = \sum h_i$  for each node.

In contrast to level-wise growth that expands all nodes at the same depth, LightGBM adopts a leaf-wise strategy: at each iteration it selects the leaf with the largest expected gain and splits only that leaf. This greedy expansion often yields stronger loss reduction under a fixed number of leaves, though it can increase overfitting risk if unconstrained. Accordingly, LightGBM typically relies on explicit controls, such as maximum depth, minimum samples per leaf, and other regularization parameters, to balance accuracy and generalization.

To further improve efficiency, LightGBM incorporates additional training accelerations. Gradient-based One-Side Sampling (GOSS) preferentially retains examples with large gradient magnitudes (which dominate the objective improvement) while subsampling low-gradient examples, reducing the effective training set size without substantially degrading optimization. Exclusive Feature Bundling (EFB) exploits sparsity by merging mutually exclusive features into a smaller set of composite features, lowering dimensionality and accelerating split search.

For multi-class settings, LightGBM commonly optimizes the cross-entropy objective with Softmax-normalized probabilities:

$$L_{multi} = -\frac{1}{n} \sum_{i=1}^n \sum_{c=1}^C y_{ic} \log p_{ic}, \quad p_{ic} = \frac{\exp(z_{ic})}{\sum_{c'} \exp(z_{ic'})} \quad (3)$$

Here,  $y_{ic}$  is the indicator for class  $c$ , and  $p_{ic}$  is the predicted probability obtained via the Softmax function.

Overall, LightGBM's combination of histogram-driven computation, greedy leaf-wise splitting, and sampling/bundling optimizations provides a practical balance between predictive strength and training efficiency, making it a strong baseline for large-scale classification tasks.

### 2.3 Bidirectional LSTM

Bidirectional long short-term memory (Bi-LSTM) extends the standard LSTM by learning temporal dependencies in both forward and backward directions, which is especially beneficial for lane-change intention prediction where preparatory cues (e.g., gradual lateral drift) and near-maneuver cues (e.g., decisive lateral velocity changes) jointly determine the intent. To strengthen representation capacity, we adopt a Bi-LSTM as the temporal feature encoder, producing a fixed-dimensional embedding that is later fused with physics-informed features in Section 2.1.

Let the input trajectory sequence within an observation window be

$$X = \{x_1, x_2, \dots, x_T\}, x_t \in \mathbb{R}^d \quad (4)$$

where  $T = H * f_s$  is the sequence length determined by observation duration  $H$  (seconds) and sampling frequency ( $f_s$ ), and  $(d)$  is the per-frame feature dimension. For each time step ( $t$ ), a standard LSTM unit computes the following gating operations:

$$f_t = \sigma(W_f[h_{t-1} + x_t] + b_f), \quad (5)$$

$$i_t = \sigma(W_i[h_{t-1} + x_t] + b_i), \quad (6)$$

$$\tilde{c}_t = \tanh(W_c[h_{t-1} + x_t] + b_c) \quad (7)$$

**Cell state** undergoes self-recursive update based on the forget gate and the input gate:

$$C_t = f_t \odot c_{t-1} + i_t \odot \tilde{c}_t \quad (8)$$

**Output gate** controls the contribution of the cell state to the current hidden state:

$$o_t = \sigma(W_o x_t + U_o h_{t-1} + b_o) \quad (9)$$

$$h_t = o_t \odot \tanh(c_t) \quad (10)$$

where  $\sigma(\cdot)$  is the sigmoid function,  $\odot$  denotes element-wise multiplication,  $c_t$  is the cell state, and  $h_t$  is the hidden state.

In this study, we employ a two-layer bidirectional LSTM (Bi-LSTM) encoder to learn a compact temporal representation of each trajectory from its sequential observations. **To this end**, we first encode the sequence in both temporal directions, **then** stack two Bi-LSTM layers to capture higher-level dynamics and **finally** apply pooling to obtain a fixed-dimensional embedding for downstream classification.

**Bidirectional encoding.** A Bi-LSTM runs two LSTMs in opposite directions. For each time step  $t$ , we obtain the forward hidden state  $\vec{h}_t$  and the backward hidden state  $\overleftarrow{h}_t$ , and concatenate them:

$$h_t^{(l)} = [\vec{h}_t^{(l)} \parallel \overleftarrow{h}_t^{(l)}], \quad (11)$$

where  $l \in \{1, 2\}$  indexes the stacked Bi-LSTM layers.

**Two-layer stacking.** The encoder adopts a two-layer stacked Bi-LSTM, where each layer uses 256 hidden units per direction. The first Bi-LSTM layer maps the raw sequence  $X$  to a sequence of bidirectional hidden states  $\{h_t^{(1)}\}_{t=1}^T$ . The second Bi-LSTM layer takes  $\{h_t^{(1)}\}$  as input and outputs higher-level temporal features  $\{h_t^{(2)}\}_{t=1}^T$ , enabling the encoder to capture more complex maneuver dynamics and longer-range dependencies than a single layer.

**Concat + pooling to form a fixed-dimensional embedding.** With the stacked features in hand, we convert the output sequence to a fixed-dimensional temporal embedding via pooling:

$$e = \text{Pool} \left( \{h_t^{(2)}\}_{t=1}^T \right), \quad (12)$$

where  $\text{Pool}(\cdot)$  can be implemented as mean pooling, max pooling, or last-step pooling (and can be substituted by attention pooling if desired). The resulting embedding  $e \in \mathbb{R}^k$  summarizes the trajectory history into a compact representation.

**Usage in the hybrid framework.** Finally, the extracted temporal embedding  $e$  is concatenated with physics-informed handcrafted features (Section 2.1) to form the fused vector  $[e \parallel f]$ , which is passed to LightGBM for final three-class intention classification (Section 2.2).

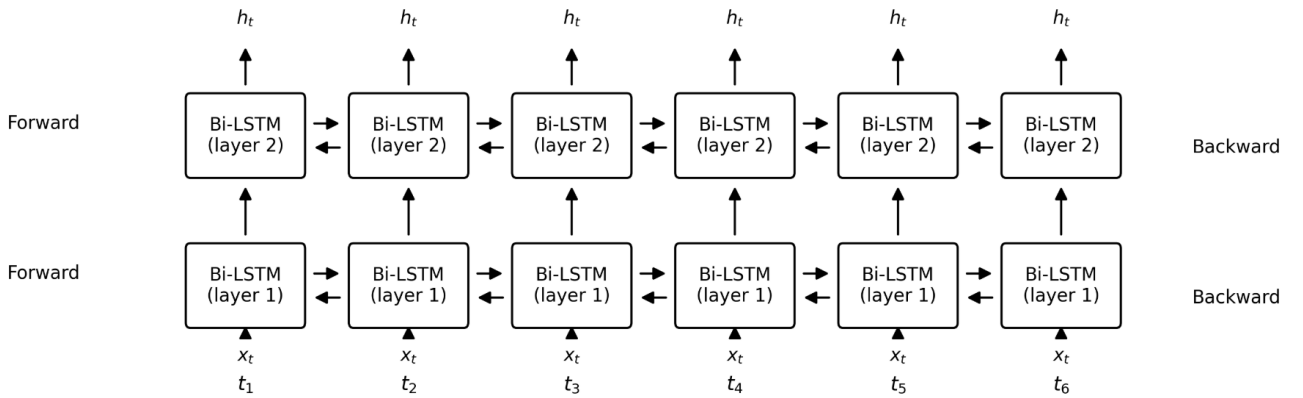


Figure 4. Bidirectional-LSTM (unrolled over time) – Sequence-to-Embedding.

### 3. DATA PROCESSING AND FEATURE EXTRACTION

#### 3.1. Overview of the highD and exiD datasets

**highD dataset.** The highD dataset is a large-scale naturalistic vehicle-trajectory corpus collected by drones over six straight highway segments in Germany. Its aerial perspective avoids occlusions and enables the extraction of over 110,000 high-accuracy trajectories, including vehicle type, size, position, and annotated maneuvers. Recorded using standardized procedures developed by RWTH Aachen’s ika institute, highD provides precise geometric data (errors typically under ten centimeters). Originally designed for validating automated driving systems, it is now widely used for highway behavior modeling, driver interaction analysis, and traffic-flow studies.

Dataset link: <https://levelxdata.com/highD-dataset/>

**exiD Dataset.** The exiD dataset follows the same drone-based recording philosophy as highD but focuses on highway on-ramp and off-ramp areas. It captures complex merging, diverging, and weaving behaviors essential for studying interaction-rich traffic. exiD includes around 69,000 trajectories from seven Autobahn sites, with detailed kinematic profiles, vehicle metadata, and map contextual information in OpenDRIVE and Lanelet2 formats. Its aerial view provides accurate, occlusion-free trajectories across free-flow and congested ramp conditions, making it valuable for automated driving safety assessment and ramp-area behavior modeling.

Dataset link: <https://levelxdata.com/exiD-dataset/>

To ensure clear supervision targets, we applied a strict maneuver-consistency rule during preprocessing. Samples containing multiple lane changes within the prediction horizon were removed, and only single-lane-change or no-lane-change trajectories were kept. This filtering reduces label noise, avoids ambiguous multi-maneuver sequences, and yields a cleaner dataset for reliable model training and evaluation.

#### 3.2. Data imbalance

Data imbalance is a major challenge for lane-change intention prediction, particularly in large-scale naturalistic datasets. The problem is especially pronounced in the highD dataset. Under a short 1-second observation window, the ratio between no lane change and left/right lane-change classes can reach 252:1. Even with a 3-second window where more maneuvers are captured, the ratio remains highly skewed at approximately 81:1, with the minority lane-change classes each comprising only 0.4%–1.2% of the samples.

By comparison, the exiD dataset exhibits a more balanced distribution, with class ratios typically in the range of 8:1:1 to 2:1:1. Due to this considerably more uniform distribution, we removed imbalance-related preprocessing steps for exiD.

To address the severe imbalance in highD, we designed a three-stage imbalance handling pipeline:

(1) SMOTE Oversampling + Tomek Links Undersampling. We first applied the SMOTE technique to synthetically oversample the minority classes. SMOTE generates new samples by interpolating between each minority instance and its  $k$  nearest neighbors in the feature space, effectively enriching rare class regions without duplicating samples.

To reduce noise and improve class separability, we then removed Tomek links, which identify borderline sample pairs where two points from different classes are each other’s nearest neighbors. Removing these samples cleans ambiguous decision boundaries.

After this procedure, the class ratio in highD was adjusted to approximately:

no-lane-change : left-lane-change : right-lane-change  $\approx 27 : 1 : 1$

(2) Inverse Frequency Class Weights in the Loss Function. To further counteract imbalance during model training, we introduced inverse frequency class weights into the loss function.

Each class  $c$  was assigned a weight:

$$w_i = \left(\frac{1}{f_c}\right) \quad (13)$$

where  $f_c$  is the normalized frequency of class  $c$ .

This forces the model to penalize errors on minority classes more heavily, preventing the network from converging toward trivial “always predict no-lane-change” behavior.

The weighting strategy significantly improved gradient contribution from the left/right lane-change classes, complementing the effects of SMOTE and Tomek preprocessing.

(3) Threshold Calibration for Minority Classes. Finally, we performed post-training threshold calibration on the validation set. Instead of applying the default 0.5 probability cutoff, we optimized class-specific thresholds to maximize macro-F1 and minority-class recall. Given the large imbalance, calibrated thresholds allowed the classifier to better distinguish subtle pre-lane-change cues and reduced under-prediction of minority classes.

After applying the above three-stage pipeline—combining SMOTE oversampling with Tomek links removal, inverse frequency class weighting, and threshold calibration—the model demonstrated substantial improvements in handling the severe class imbalance in the highD dataset. The overall macro-F1 score increased by an average of 24 points, reflecting more balanced performance across all classes. Moreover, recall for the minority classes improved significantly, with left lane-change recall increasing by approximately 37% and right lane-change recall rising by around 32%. These results confirm that the integrated imbalance-mitigation strategy effectively strengthened the model’s ability to detect rare but safety-critical lane-change intentions.

### 3.3. Feature extraction

This study conducts extensive feature engineering on two large-scale naturalistic vehicle trajectory datasets—highD and exiD—both offering detailed kinematic and geometric representations of highway traffic. To support real-time lane-change intention recognition, we implemented a standardized preprocessing pipeline encompassing data cleaning, temporal synchronization, and feature expansion based on temporal statistics and spatial semantics. The final feature matrices consist of 243 variables for highD (27 fundamental and 216 derived) and 264 variables for exiD (28 fundamental and 236 derived). To ensure methodological transparency and scalability, all extracted features are categorized into five physics-informed groups as defined in Section 2.1:

1. Kinematics and temporal statistics. Based on the trajectory of the vehicle’s center point, we calculate scalar speed, acceleration magnitude, heading angle, yaw rate, and curvature radius. To further capture transient driving trends and stability, we extract short-term dynamics by computing rolling-window statistics—including the mean, standard deviation, and extrema of speed, acceleration, and yaw angle within a 1-second window. In addition, for key kinematic variables such as speed, velocity, and acceleration, we expand the temporal representation using a family of multi-scale sequence descriptors. These include multi-scale lagged differences (0.5–2 seconds), exponential moving averages and EMA slopes, short-window autocorrelation, spectral energy ratios, zero-crossing rates, linear-fit  $R^2$  scores, TTC-threshold event statistics, run-length measures of sustained motion, cumulative lateral energy, and time-to-boundary indicators. Together, these enriched temporal features capture trends, volatility, periodicity, and change-point signals essential for anticipating early lane-change intentions.
2. Lane geometry and positioning. From the provided lane identifiers, boundary coordinates, and centerline data, we compute lateral offsets, distances to boundaries, and their temporal derivatives. In addition, rolling-window averages and absolute displacements are derived to represent lane-keeping stability and the preparatory motion preceding lane changes.
3. Interaction with surrounding vehicles. Using the neighbor indices embedded in the datasets, we model each vehicle’s local traffic topology and determine relative longitudinal and lateral gaps, velocity and acceleration differences, as well as approach rates for six principal neighboring positions (front, rear, left, right, and diagonals). To capture surrounding traffic congestion, we further calculate the spatial occupancy ratio of adjacent vehicles.

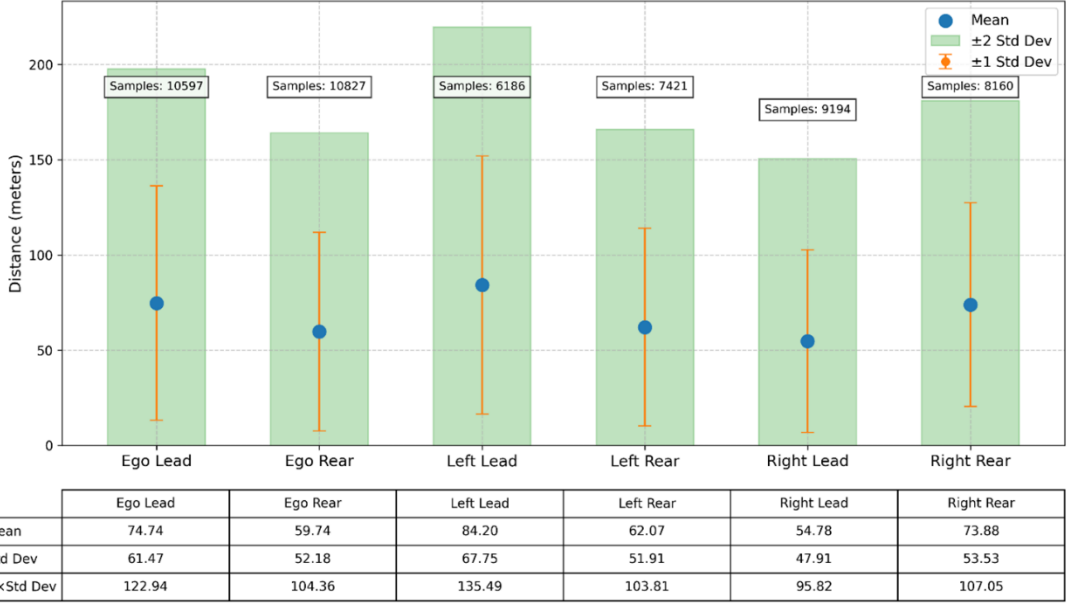


Figure 5. Average distance and distribution statistics between the lane-changing vehicle and adjacent vehicles (based on the highD dataset).

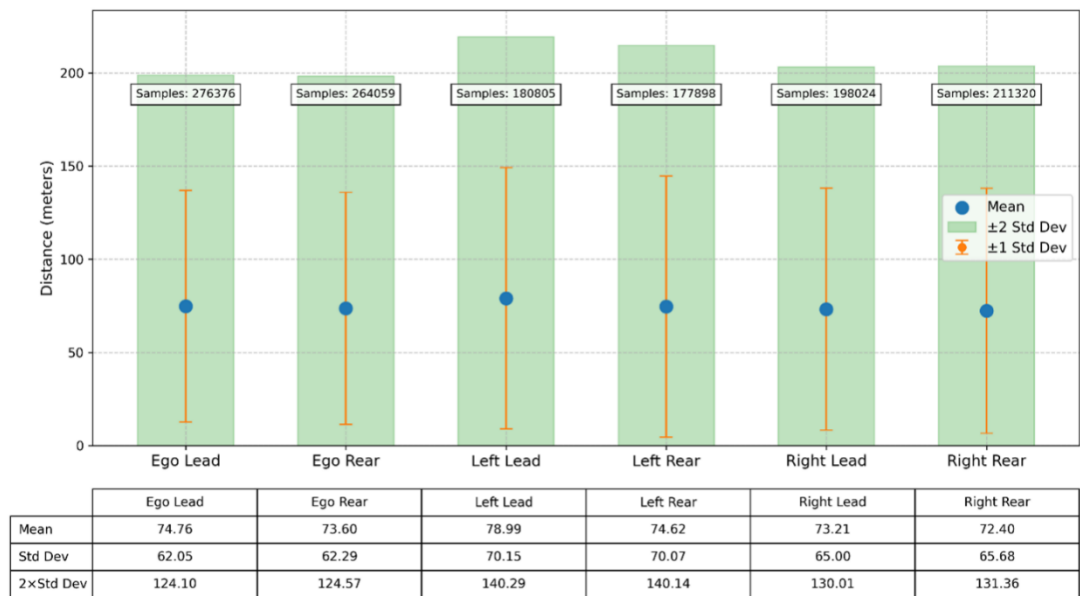


Figure 6. Average distance and distribution statistics between the lane-changing vehicle and adjacent vehicles (based on the exiD dataset).

Figures 5 and 6 depict the lateral spacing between the ego vehicle and its surrounding participants (front, rear, and adjacent-lane vehicles) at the instant of lane change for both the highD and exiD datasets. For example, in Figure 5, the typical spacing varies between 54.8 m and 84.2 m, with a standard deviation of 47.9–67.8 m. The light-green band represents a  $\pm 2\sigma$  interval, whereas the orange band denotes  $\pm 1\sigma$ , empirically characterizing acceptable safety margins. Beyond the

pairwise interaction variables, this distributional information—when combined with neighbor indices—enables the derivation of several higher-level indicators:

(a) Normalized distance distribution. For each distance  $d_i$ , we computed:

$$z_i = \frac{d_i - \mu_i}{\sigma_i}, s_i = \frac{d_i}{\mu_i} \quad (14)$$

Where  $\mu_i$  and  $\sigma_i$  are the mean and standard deviation of Figure 5 and Figure 6, respectively. The metric  $z_i$  reduces scale bias due to roadway or traffic flow differences, while  $s_i$  preserves relative spacing information.

(b) Safe gap indicator. A distance is considered safe if  $d_i > \mu_i + 2\sigma_i$  (beyond the upper bound of the green region).

$$g_i = \begin{cases} 1, & \text{if safe} \\ 0, & \text{otherwise} \end{cases}, \sum_i g_i \text{ gives the number of safe gap.} \quad (15)$$

(c) Lane advantage index:

$$\Delta_{\text{lead}} = d_{\text{LeftLead}} - d_{\text{EgoLead}}, \Delta_{\text{rear}} = d_{\text{LeftRear}} - d_{\text{EgoRear}} \quad (16)$$

We define  $\min(\Delta_{\text{lead}}, \Delta_{\text{rear}})$  as the overall availability score for the adjacent lane. A positive value indicates that the neighboring lane provides larger longitudinal gaps, implying higher feasibility for a lane change.

(d) Time-to-gap measure. The spacing  $d_i$  is divided by the ego vehicle's velocity, producing the residual following time  $t_i = d_i/v_{\text{ego}}$ . Applying z-score normalization to  $t_i$  provides a velocity-independent temporal measure of gap availability.

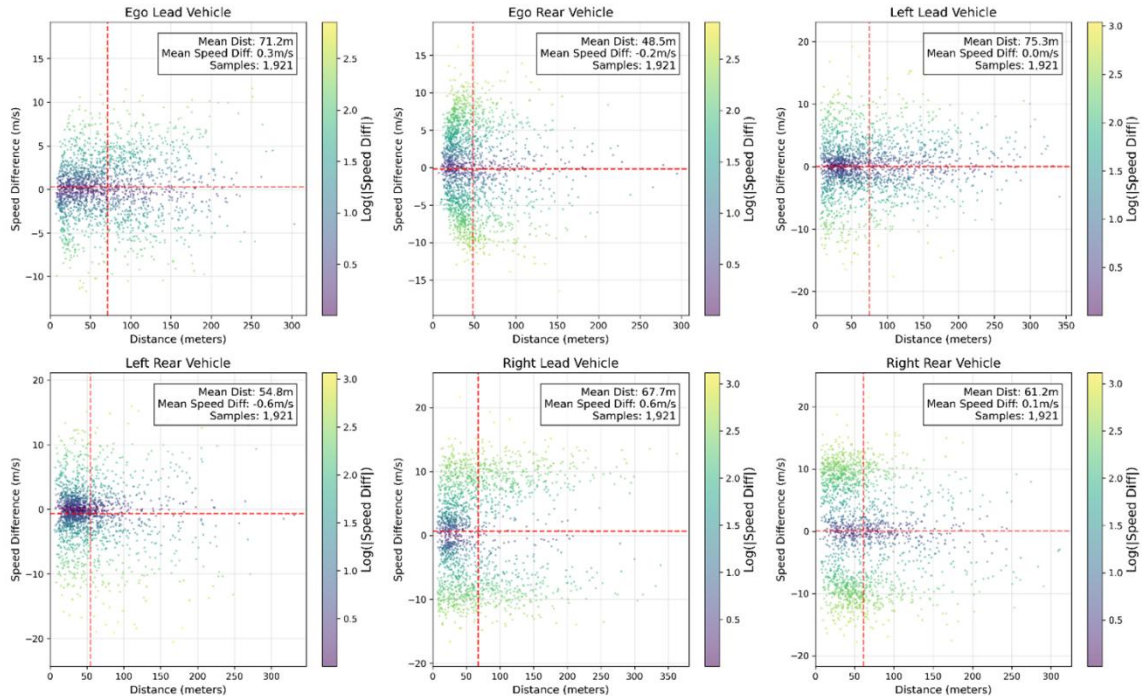


Figure 7. Distance-speed difference distribution (based on the highD dataset).

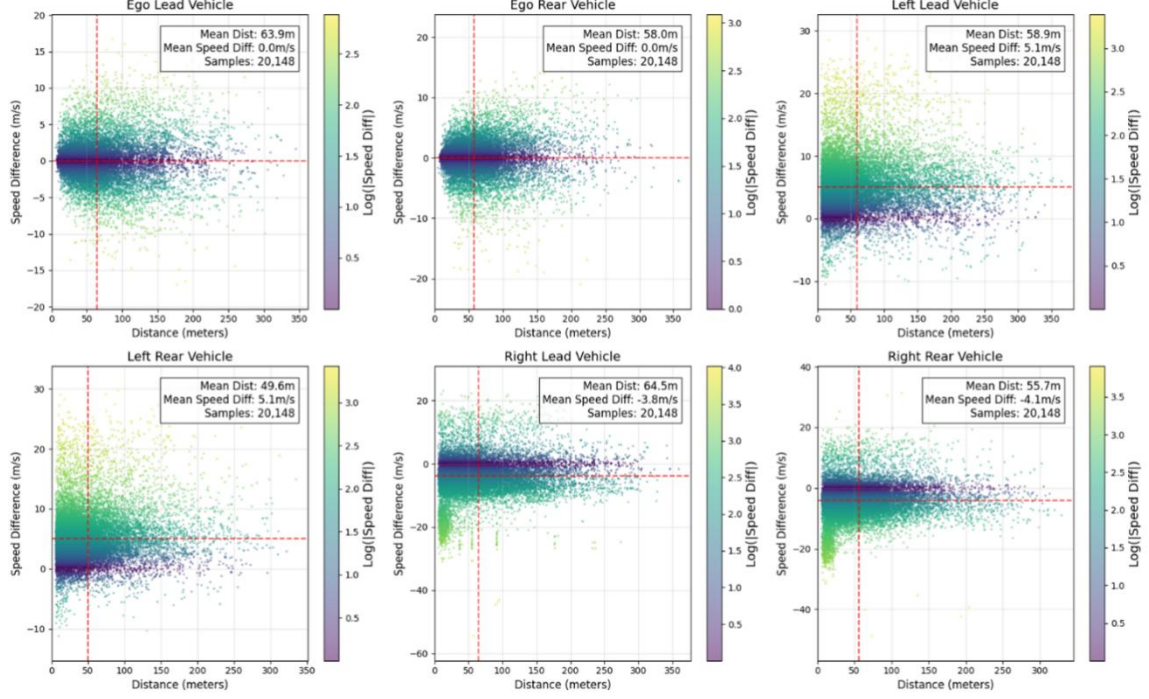


Figure 8. Distance-speed difference distribution (based on the exiD dataset).

Figures 7 and 8 depict the joint distribution of lateral distances and relative velocity differences between the ego vehicle and its six surrounding neighbors during lane-change events. Most observations concentrate near zero relative velocity, while a smaller cluster corresponds to the short-distance/high-speed-difference region, representing potentially risky situations.

To transform this two-dimensional relationship into a single learnable feature, we define the Closing Gap Time (CGT) for each neighboring vehicle  $i$ :

$$CGT_i = \frac{d_i}{|\Delta v_i| + \varepsilon} \quad (17)$$

where  $d_i$  is the lateral distance,  $\Delta v_i$  the relative speed between the ego and neighbor vehicles, and  $\varepsilon$  a small stabilizing constant. CGT directly reflects the time required for the current speed difference to close the gap, thereby serving as an indicator of lane-change safety margins (with smaller values indicating higher risk).

4. Longitudinal safety features. We also integrate several classic longitudinal risk metrics, including Distance Headway (DHW), Time Headway (THW), and Time-to-Collision (TTC). For each measure, we record the minimum value within the observation window, employing it as either a soft or hard safety constraint in the learning objective.

5. Behavioral semantics. To capture driver intent and behavioral tendencies, we extract descriptive variables such as vehicle type, lane-change frequency, posted speed limits, instantaneous velocity, velocity ratios, and acceleration ratios. These indicators encode driver-specific traits, such as aggressiveness, assertiveness, or caution, that influence lane-change decisions.

In addition, the exiD dataset offers extended metadata derived from OpenDRIVE roadway annotations, enabling the incorporation of ramp-related descriptors (e.g., distances to entry and exit points, estimated time-to-arrival) and multi-horizon indicators at 5 s, 15 s, and 30 s. These supplemental features substantially improve the model's capacity to interpret lane-change feasibility in complex merging or diverging traffic conditions.

## 4. EXPERIMENTS

### 4.1. Experimental setup

To investigate how the duration of historical observations and the choice of prediction horizon influence lane-change intention modeling, we carried out a set of controlled experiments using the highD and exiD naturalistic trajectory datasets. To maintain a strict separation between training and evaluation data and to eliminate any potential overlap in vehicle trajectories, we split both datasets according to their recording locations. For highD, samples from locations 0, 1, 2, and 3 were assigned to the training set, while locations 4 and 5 served exclusively as the test set. A similar location-based split was applied to exiD, where data from locations 0, 1, 2, and 3 were used for model training and those from locations 4, 5, and 6 were held out for testing.

Prior to model training, all configurations were optimized through Bayesian hyperparameter search combined with a 5-fold cross-validation routine, allowing the parameter space to be explored effectively under constrained computational resources.

To thoroughly examine the relationship between observation length and predictive accuracy, we tested a wide range of history window sizes under prediction horizons of 1 s, 2 s, and 3 s. The history window for highD was varied from 1 to 5 seconds, while exiD experiments covered window lengths from 2 to 7 seconds, ensuring that all practically meaningful intervals were included. For each prediction horizon  $T$ , we evaluated every candidate window length  $W$ , recorded performance on both training and held-out data, and subsequently determined the window size that yielded the best generalization performance for the specified horizon.

### 4.2. Performance across historical windows, prediction horizons, and models

#### 4.2.1. LightGBM results

For the highD dataset, the most effective configuration was obtained with a short historical window of  $W=1$  second. Under this setting, the model reached generalization accuracies of 0.9981, 0.9952, and 0.9906 for prediction horizons of  $T=1$ , 2, and 3 seconds, respectively. The corresponding Macro F1-scores were 0.9359, 0.9126, and 0.8761. As summarized in Table 1, the No-LC class maintained near-perfect F1-scores across all horizons, whereas the Left-LC and Right-LC categories exhibited noticeable reductions, particularly at the longer 2-second and 3-second prediction horizons.

In contrast, the exiD dataset favored a considerably longer historical context, with the optimal window identified as  $W=6$  seconds. Using this window, the model achieved generalization accuracies of 0.9607, 0.8950, and 0.8117 for  $T=1$ , 2, and 3 seconds. The corresponding Macro F1-scores were 0.9004, 0.8343, and 0.7819. Both metrics showed a consistent downward trend as the prediction horizon increased, with performance deteriorating most prominently at the 3-second horizon.

#### 4.2.2. Two-layer stacked LSTM results

For the highD dataset, the optimal history window was  $W = 2$ s. Under these settings, the generalization accuracies were 0.9970, 0.9934, and 0.9875 for the three horizons, with Macro F1-scores of 0.9162, 0.8847, and 0.8430, respectively (Table 2). Similar to LightGBM, the No-LC class maintained near-perfect F1, while Left-LC and Right-LC recognition performance declined at  $T = 2$ s and  $T = 3$ s.

On the exiD dataset, the best history windows were  $W = 4$ s for  $T = 1$ s and 2s, and  $W = 5$ s for  $T = 3$ s. The corresponding generalization accuracies were 0.8705, 0.7742, and 0.7058, with Macro F1-scores of 0.7702, 0.7233, and 0.6875. As summarized in Table 2, performance consistently decreased with longer prediction horizons, and the declines were particularly pronounced for the Left-LC and Right-LC classes.

Table 1. Optimal performance of LightGBM across different prediction horizons.

Dataset	Prediction Horizon	Overall Accuracy	Macro F1	NO-LC F1	Left-LC F1	Right-LC F1
highD	1s	0.9981	0.9359	0.9990	0.8999	0.9087
highD	2s	0.9952	0.9126	0.9975	0.8588	0.8815
highD	3s	0.9906	0.8761	0.9951	0.8017	0.8315
exiD	1s	0.9607	0.9004	0.9895	0.8512	0.8606
exiD	2s	0.895	0.8343	0.9755	0.7465	0.781

exID	3s	0.8117	0.7819	0.9284	0.7025	0.7148
------	----	--------	--------	--------	--------	--------

Table 2. Optimal performance of the Bi-LSTM across different prediction horizons.

Dataset	Prediction Horizon	Overall Accuracy	Macro F1	NO-LC F1	Left-LC F1	Right-LC F1
highD	1s	0.9970	0.9162	0.9981	0.8715	0.8790
highD	2s	0.9934	0.8847	0.9964	0.8024	0.8553
highD	3s	0.9875	0.8430	0.9930	0.7399	0.7961
exID	1s	0.8704	0.7702	0.9284	0.6717	0.7104
exID	2s	0.7742	0.7233	0.8657	0.6462	0.6579
exID	3s	0.7058	0.6875	0.8020	0.6264	0.6341

Table 3. Optimal performance of the Temporal Model across different prediction horizons.

Dataset	Prediction Horizon	Overall Accuracy	Macro F1	NO-LC F1	Left-LC F1	Right-LC F1
highD	1s	0.9970	0.9162	0.9981	0.8715	0.8790
highD	2s	0.9934	0.8847	0.9964	0.8024	0.8553
highD	3s	0.9875	0.8430	0.9930	0.7399	0.7961
exID	1s	0.8704	0.7702	0.9284	0.6717	0.7104
exID	2s	0.7742	0.7233	0.8657	0.6462	0.6579
exID	3s	0.7058	0.6875	0.8020	0.6264	0.6341

#### 4.3. Evaluation and analysis

From the overall results, two factors stand out as the primary determinants of model performance: the prediction horizon (T) and the complexity of the traffic scene.

##### 4.3.1 Effect of prediction horizon

Across all three model families and both datasets, performance degrades as the prediction horizon T increases from 1 s to 3 s. This trend is evident in both overall accuracy and Macro F1, but is more pronounced for the minority classes Left-LC and Right-LC.

For the highD dataset, all models maintain very high accuracies even at T=3 s, but the Macro F1-scores show a gradual decline. The near-perfect recognition of the No-LC class indicates that stable lane-keeping can be reliably identified several seconds in advance. However, correctly forecasting lane-change maneuvers becomes increasingly difficult as the time-to-maneuver grows, since driver decisions and local traffic conditions can change rapidly within a 2–3 s window.

On the exID dataset, the deterioration with longer horizons is more substantial. While performance at T=1 s remains strong, both accuracy and Macro F1 drop notably at T=2 s and especially at T=3 s. This reflects the higher uncertainty in ramp and merging regions, where interactions with multiple surrounding vehicles and infrastructure can cause abrupt changes in maneuver plans. At longer horizons, small variations in traffic context can result in divergent outcomes, making early predictions more error-prone.

These results highlight an inherent trade-off between anticipation and reliability: shorter horizons provide more accurate and balanced predictions, whereas longer horizons offer earlier warnings but at the cost of decreased F1-scores for lane-change classes.

##### 4.3.2 Model comparison and benefits of the hybrid temporal framework

Comparing the three model families reveals clear advantages of the proposed LightGBM + Bi-LSTM temporal framework. On both highD and exID, the hybrid model consistently surpasses the standalone LightGBM and Bi-LSTM baselines in terms of Macro F1 across all prediction horizons, while maintaining or slightly improving overall accuracy.

On the highD dataset, the hybrid model yields the highest Macro F1 at all horizons, indicating a better balance between the majority No-LC and the minority lane-change classes. This suggests that combining high-level temporal embeddings

with physics-informed handcrafted features allows the model to capture subtle pre-maneuver dynamics more effectively than either component alone.

On the exiD dataset, the hybrid approach offers even more pronounced gains, particularly at longer horizons. While the Bi-LSTM alone tends to underperform the LightGBM baseline in both accuracy and Macro F1, the hybrid model outperforms both, demonstrating that the temporal features extracted by the Bi-LSTM become significantly more useful once they are fused with structured physical semantics and exploited by a tree-based classifier that can model complex, non-linear feature interactions under class imbalance.

#### 4.3.3 Class-wise behavior and dataset difficulty

A consistent pattern across all experiments is that the No-LC class is predicted with near-perfect F1-scores on both datasets and across all horizons. This is expected given its majority status and the relative stability of lane-keeping behavior. In contrast, the Left-LC and Right-LC classes exhibit systematically lower F1-scores, with sharper declines as T increases.

The performance gap between highD and exiD further underscores the increased difficulty of predicting lane-change maneuvers in ramp-rich environments. Even when using the best-performing historical windows and the hybrid model, the Macro F1 on exiD remains lower than that on highD, especially for 2 s and 3 s horizons. This indicates that exiD presents a more challenging multi-scenario prediction problem, characterized by heterogeneous behaviors, denser interactions, and higher uncertainty about future maneuvers.

From an application perspective, these findings imply that model configuration should be environment-specific. On relatively straight highway segments (highD), shorter observation windows and moderate prediction horizons can deliver both early and reliable predictions. In contrast, in ramp and merging regions (exiD), the system may require longer histories and possibly shorter operational horizons (or probabilistic risk estimates) to maintain acceptable reliability for safety-critical use cases.

#### 4.3.4. Summary

Overall, the experimental results yield three principal observations:

##### 1. Influence of prediction horizon.

Across all model configurations and both datasets, predictive performance systematically deteriorates as the horizon extends from 1 s to 3 s. This degradation is especially pronounced for the Left-LC and Right-LC classes, underscoring an inherent trade-off between early anticipation of lane-change maneuvers and the reliability of class-wise discrimination.

##### 2. Effect of model architecture.

The proposed hybrid LightGBM + Bi-LSTM temporal framework consistently achieves superior performance relative to the standalone LightGBM and Bi-LSTM baselines, particularly in terms of Macro F1. By integrating high-level temporal representations with physics-informed handcrafted features, the hybrid model attains a more favorable balance between overall accuracy and minority-class recognition, especially under class-imbalanced conditions.

##### 3. Role of dataset complexity and traffic context.

The exiD dataset poses a substantially more challenging prediction task than highD, as reflected by lower Macro F1-scores and stronger sensitivity to the prediction horizon. This difference highlights the impact of ramp-rich, interaction-intensive environments on maneuver predictability and emphasizes the necessity of context-aware model design and parameterization for deployment in heterogeneous highway scenarios.

## 5. CONCLUSION AND FUTURE WORK

This study proposed a temporal physics-informed framework for three-class lane-change intention prediction on multi-scenario highways and conducted a systematic evaluation on the highD and exiD datasets. By combining Bi-LSTM-based temporal embeddings with physics-guided handcrafted features in a hybrid LightGBM + Bi-LSTM model, we consistently achieved higher Macro F1 than strong LightGBM and Bi-LSTM baselines, while maintaining high overall accuracy. The experiments showed that shorter historical windows are sufficient on straight highway segments, whereas ramp-rich scenarios benefit from longer temporal context, and that performance degrades as the prediction horizon increases, especially for the Left-LC and Right-LC classes.

Several limitations of the present work open up concrete directions for future research. First, our analysis is restricted to single lane-change or no-lane-change trajectories after filtering out samples with multiple maneuvers; extending the framework to handle more complex patterns such as successive lane changes, aborted maneuvers, and cut-ins would better reflect real-world driving behavior and enable finer-grained maneuver taxonomies. Second, both training and evaluation are based on German highway data; future work will investigate cross-domain generalization to other countries, road geometries (e.g., urban arterials, ring roads, weaving sections), and different traffic regulations, potentially leveraging domain adaptation or transfer learning to mitigate distribution shifts. Third, the current models provide point predictions; incorporating calibrated uncertainty estimates and risk-sensitive decision thresholds would support safer integration into planning and control modules. Finally, enriching the physics-informed feature set with additional modalities, such as camera, radar, or V2X information, and exploring continual or online learning schemes to adapt to evolving traffic patterns represent promising directions to further enhance robustness and practical applicability in intelligent transportation systems.

In summary, this work demonstrates that a physics-informed hybrid temporal framework can substantially improve multi-scenario lane-change intention prediction, while also providing a foundation for future extensions toward richer maneuver taxonomies, multi-modal inputs, uncertainty-aware prediction, and cross-domain deployment in intelligent transportation systems.

## REFERENCES

- [1] M. Shawky, "Factors affecting lane change crashes," *IATSS Res.* 44(2), 155–161 (2020). <https://doi.org/10.1016/j.iatssr.2019.12.002>
- [2] T. Toledo, H. N. Koutsopoulos, and M. Ben-Akiva, "Integrated driving behavior modeling," *Transportation Research Part C*, 15(2), 96–112 (2007). <https://doi.org/10.1016/j.trc.2007.02.002>
- [3] A. Kesting, M. Treiber, and D. Helbing, "General lane-changing model MOBIL for car-following models," *Transportation Research Record*, 1999(1), 86–94 (2007). <https://doi.org/10.3141/1999-10>
- [4] Z. Zheng, "Recent developments and research needs in modeling lane-changing behavior," *Transportation Research Part B*, 60, 16–32 (2014). <https://doi.org/10.1016/j.trb.2013.11.009>
- [5] H. Qi, C. Chen, X. Hu, and J. Zhang, "Online inference of lane changing events for connected and automated vehicle applications with analytical logistic diffusion stochastic differential equation," *Transportation Research Part C*, 144, 103874 (2022). <https://doi.org/10.1016/j.trc.2022.103874>
- [6] R. Izquierdo, I. Parra, D. Fernandez-Llorca, and M. A. Sotelo, "Experimental validation of lane-change intention prediction based on action recognition network," *IEEE ITSC* (2019). <https://doi.org/10.1109/ITSC.2019.8917331>
- [7] Q. Shi and H. Zhang, "An improved learning-based LSTM approach for lane change intention prediction subject to imbalanced data," *Transportation Research Part C*, 133, 103414 (2021). <https://doi.org/10.1016/j.trc.2021.103414>
- [8] J. C. Hayward, *Near-Miss Determination Through Use of a Scale of Danger*, Highway Research Record 384 (1972). <https://onlinepubs.trb.org/Onlinepubs/hrr/1972/384/384-004.pdf>
- [9] K. Vogel, "A comparison of headway and time to collision as safety indicators," *Accident Analysis & Prevention*, 35(3), 427–433 (2003). [https://doi.org/10.1016/S0001-4575\(02\)00022-2](https://doi.org/10.1016/S0001-4575(02)00022-2)
- [10] J. H. Friedman, "Greedy function approximation: A gradient boosting machine," *Annals of Statistics*, 29(5), 1189–1232 (2001). <https://doi.org/10.1214/aos/1013203451>
- [11] A. Natekin and A. Knoll, "Gradient boosting machines, a tutorial," *Frontiers in Neurorobotics*, 7, 21 (2013). <https://doi.org/10.3389/fnbot.2013.00021>